Transition metal oxides as hole-selective contacts in silicon heterojunctions solar cells

Luis G. Gerling [a,b,*] , Somnath Mahato [a,b,1] , Anna Morales-Vilches [a], Gerard Masmitja [a], Pablo Ortega [a], Cristobal Voz [a], Ramon Alcubilla [a,b], Joaquim Puigdollers [a,b]

[a] Dept. Enginyeria Electrònica, Universitat Politècnica de Catalunya, Jordi Girona 1-3, Barcelona 08034, Spain

[b] Centre de Recerca en Nanoenginyeria (CrNE), Pascual Vila 15, Barcelona 08028, Spain

Abstract

This work reports on a comparative study comprising three transition metal oxides, MoO_3, WO_3 and V_2O_5, acting as front p-type emitters for n-type crystalline silicon heterojunction solar cells. Owing to their high work functions (>5 eV) and wide energy band gaps, these oxides act as transparent hole-selective contacts with semiconductive properties that are determined by oxygen-vacancy defects (MoO_{3-x}), as confirmed by x-ray photoelectron spectroscopy. In the fabricated hybrid structures, 15 nm thick transition metal oxide layers were deposited by vacuum thermal evaporation. Of all three devices, the V_2O_5/n-silicon heterojunction performed the best with a conversion efficiency of 15.7% and an open-circuit voltage of 606 mV, followed by MoO_3 (13.6%) and WO_3 (12.5%). These results bring into view a new silicon heterojunction solar cell concept with advantages such as the absence of toxic dopant gases and a simplified low-temperature fabrication process.

Keywords: silicon heterojunction; transition metal oxide; carrier selective contact

* Corresponding author. Tel.: +34 93 401 1002; Fax: +34 93 401 6756; E-mail address: guillermo.gerling@upc.edu

[1] Present address: Dept. of Applied Physics, Indian School of Mines, Dhanbad 826004, India

1. Introduction

The last years much effort has been devoted by the photovoltaic community to find crystalline silicon (c-Si) solar cell technologies with competitive manufacturing costs. Cost reduction strategies include using ultra-thin wafers or lower-quality substrates, but in any case lower thermal budgets and simplified fabrication processes would be desirable. In this regard, silicon heterojunction structures constitute a cornerstone where low-temperature manufacturing and high conversion efficiency can be combined. Concepts such Panasonic's back-contact HIT (Heterojunction with Intrinsic Thin layer) combine excellent surface passivation with hole/electron-selective contacts deposited at low-temperature, achieving record efficiencies of 25.6% [1]. Nonetheless, the p/n-doped hydrogenated amorphous silicon (a-Si:H) stacks are deposited by Plasma-Enhanced Chemical Vapor Deposition (PECVD), a capital-intensive system with mandatory security systems considering the flammable and toxic boron/phosphorous gas precursors employed. In this sense, the utilization of risk-free materials deposited at low temperature is a comprehensive alternative to further decrease production costs.

Subsequently, recent research on organic thin-film photovoltaics has provided a considerable number of carrier-selective materials (i.e. with preferential conductivity for either electrons or holes) which can be deposited by low-temperature or solution processes. Besides allowing the effective separation of carriers, these alternative materials must provide low surface recombination velocities and negligible contact resistivities if they were to replace traditional dopants in silicon. For instance, organic semiconductor materials such as P3HT and PEDOT:PSS have recently attracted much attention in organic/inorganic photovoltaic devices, based on their demonstrated hole injection and extraction properties when used as buffer layers in organic photovoltaics [2]. Hybrid c-Si/organic structures where the p-doped layer is replaced by PEDOT:PSS have already been demonstrated [3,4], achieving an outstanding open-circuit voltage (V_{OC}) of 657 mV and a conversion efficiency above 20% [5]. Yet, PEDOT:PSS suffers from chemical instability related to its hygroscopic character and can cause severe device degradation [6]. A variety of p-type polymeric semiconductors have also been studied for silicon hybrid devices [7,8], although they could suffer from similar instability issues.

Another kind of materials that have demonstrated excellent carrier-selective properties are transition metal oxides (TMOs), wide bandgap semiconductors with a distinctive p- or n-type

character and a broad range of work functions varying from 2 to 7 eV [9]. Many reports can be found in the literature regarding interface engineering with TMOs applied to organic light emitting diodes (OLEDs) and organic solar cells [10], such as molybdenum trioxide (MoO_3) [11], tungsten trioxide (WO_3) [12], vanadium pentoxide (V_2O_5) [13] and rhenium trioxide (ReO_3) [14]. These TMOs work as hole-selective contacts due to their large work functions (>5 eV) laying close to the Highest Occupied Molecular Orbital (HOMO) level of several p-type organic semiconductors, favoring ohmic contact formation. Since TMOs are more stable than their organic counterparts [15] and possess the same low-temperature and solution-based processability, it is natural to explore their potential as doping alternatives for c-Si solar cells. However, research on the incorporation of TMOs into silicon devices dates from very recent years [16,17]. Particularly, heterojunction solar cells based on p-type c-Si (p-Si) and TMOs acting as p-type Back Surface Fields (BSFs) were reported recently [18,19], demonstrating low contact resistivities and efficiencies of 15%. Furthermore, the use of TMOs as p-type emitters in n-type c-Si (n-Si) has also been investigated for MoO_3 [18,20,21] and WO_3 [22], demonstrating a power conversion efficiency of 18.8% for this novel solar cell concept [23].

In this work we comparatively study three transition metal oxides (V_2O_5, MoO_3 and WO_3) acting as hole-selective contacts in n-type c-Si solar cells, of which V_2O_5 is the first case to be reported. Although these TMOs have similar functionality, differences in their optical and electronic properties will be shown. Special emphasis will be put on their capability to passivate c-Si surfaces without the influence of additional passivation interlayers (such as intrinsic a-Si:H) in order to objectively compare their potential as p-type emitter alternatives.

2. Experimental methods

Surface composition of the TMOs was determined by X-ray Photoelectron Spectroscopy (XPS). Samples were prepared on flat n-Si wafers previously conditioned by standard RCA cleaning [24], followed by 1% HF dip for 1 min. Then, powdered V_2O_5, MoO_3 and WO_3 (>99.99% purity, Sigma Aldrich) were thermally evaporated in vacuum (~$8x10^{-6}$ mbar) from a tantalum boat upon the room temperature substrates. The deposition rate was ~0.2 Å/s, as controlled by quartz micro-balance previously calibrated with Scanning Electron Microscope (SEM) measurements of lamella samples. Since the probing depth in XPS is only a few nanometers, a 15 nm transition metal oxide thickness was chosen to representatively characterize the oxide without the influence of Si/metal-oxide interactions [25]. After a brief exposure to air, samples were transferred from the evaporation chamber into the XPS system

(SPECS, Germany) and left for 18 hours under ultra-high vacuum (<$3x10^{-9}$ mbar) to improve analysis quality. Scans were performed using a non-monochromated Al-Kα X-ray excitation source at 1486.6 eV, detecting photoelectrons (Phoibos 150 MCD-9 detector) at a 25 eV pass energy in 0.1 eV steps. All binding energies were referred to the C1*s* binding energy level (284.8 eV) for internal reference. Further TMO characterization included spectrophotometry measurements (Shimadzu UV3600) on soda-lime glass slides and lateral resistivity measurements between two gold electrodes (length/width = 0.01 mm/mm) deposited upon an insulating SiO_2/c-Si surface.

The structure of the TMO/n-Si heterojunction solar cells fabricated with V_2O_5, MoO_3 and WO_3 is depicted in Fig. 1(a), while Fig. 1(b) summarizes the main processing steps. Float Zone (100) n-Si wafers (1.5 Ω·cm, 280 μm thick) were randomly-texturized by alkaline etching and cleaned by RCA and 1% HF dipping. The substrates were immediately loaded into a PECVD system (Elettrorava, Italy) to deposit a stack of layers on the rear side. This stack consisted of a 4 nm intrinsic a-SiC_x:H (x~0.2) passivation layer, a 15 nm phosphorous-doped a-Si:H layer and a 80 nm a-SiC_x:H (x~1) back reflector. Then, the rear side was laser-fired to obtain an array of locally-diffused point contacts (0.5% contacted area fraction) [26], resulting in a highly passivated back contact with contact resistivities <1 mΩ·cm^2. After a second 1% HF dip, the TMOs were thermally evaporated on the front side (~$8x10^{-6}$ mbar, ~0.2 Å/s), of which WO_3 has the highest melting point (1,470 ºC) compared to V_2O_5 and MoO_3 (690 and 790 ºC respectively). After a brief air exposure, an antireflective indium-tin-oxide (ITO) front electrode was deposited by RF magnetron sputtering, measuring the photoconductance of the samples (Sinton Instruments) before and after ITO deposition. After lithographic patterning of 1 cm^2 active cell areas, back-contact metallization was done by e-beam evaporation of titanium (15 nm) and thermal evaporation of aluminum (1 μm), whereas the front-contact silver grid (50 μm wide fingers, 4.3% shadow) was thermally evaporated. As a reference, a device with an a-Si:H emitter was fabricated in parallel.

The current density-voltage (*J–V*) characteristics of the fabricated solar cells were measured in the dark and under 1 sun illumination (Oriel Instruments solar simulator, calibrated by pyranometer), while the External Quantum Efficiency (EQE) was measured by means of an EQE measurement system (QEX10, PV Measurements). A 4 cm^2 area of the finished device was left without the front grid in order to measure the total reflectance by spectrophotometry with an integrating sphere.

3. Results and discussion

3.1 Properties of Transition Metal Oxides

The adequacy of V_2O_5, MoO_3 and WO_3 as large work function carrier-selective materials depends on their specific electronic properties. Although they once were misidentified as p-type semiconductors, their n-type character is now generally accepted. Such n-type semiconductivity generates from intrinsic oxygen vacancies in their atomic structure (i.e. MoO_{3-x}), ranging from insulators in their fully stoichiometric configuration (MoO_3) to metallic-like conductors (MoO_2). Since their energy band gap (E_{gap}) lies within the O2*p*- and metal *d*-bands, it is the occupancy of these *d*-states what determines their conductivity and work function value [9].

Oxidation state transitions and generation of states within the E_{gap} have been reported as characteristic features of oxygen loss during TMO deposition [27]. In order to identify such vacancy-related effects, the XPS photoemission spectra were analyzed. After Shirley background subtraction and fitting by Gaussian-Lorentzian curves, a multi-peak deconvolution of the spectra was performed by use of the binding energies referenced in the literature, allowing to quantify the relative content of each oxidation state and the oxygen to metal (O/M) ratios from the integrated peak areas. Since the samples were briefly exposed to air (~1 min.), some contamination of the uppermost atomic layers was measured as adventitious C-OH compounds and subtracted from the overall oxygen content. The core level spectra for the three oxides under study are shown in Fig. 2, while Table 1 summarizes their composition and O/M ratios. For V_2O_5, the V2*p* core level was decomposed into two doublet peaks centered at 518.1 and 516.5 eV binding energies, with a doublet spin-orbit splitting Δ_{BE} = 7.6 eV and a peak area ratio of 2:1. These characteristic binding energies are attributed to the presence of both V^{+5} and V^{+4} cations [28], as shown in Fig. 2(a). The V^{+4} fraction in the overall composition was estimated at 3.1%, while an O/M ratio of 2.29 results in an oxygen-deficient V_2O_{5-x} with x ~0.4. Similarly, the Mo3*d* core level was deconvoluted into two doublets centered at 233.4 and 231.8 eV (Δ_{BE} =3.1 eV, 3:2 area ratio), representative of Mo^{+6} and Mo^{+5} respectively [29] as shown in Fig. 2(b). The oxygen deficiency in MoO_{3-x} was calculated at x ~0.5, with a 0.5% relative content of Mo^{+5} cations in the total composition. Thirdly, the W4*f* core level of WO_3 was also decomposed into two doublets centered at 36.8 and 34.8 eV (Δ_{BE} =2.2 eV, 4:3 area ratio), characteristic of W^{+6} and W^{+5} cations [30]. However, the peak for the W^{+5} doublet was almost absent, as seen in Fig. 2(c). This is

supported by an O/M ratio that results in an oxygen-rich $WO_{3.2}$, contrary to the observed oxygen deficiency in V_2O_x and MoO_x. This fact is explained by the specific pressure conditions under which oxygen loss occurs in thermally evaporated WO_3 [31]. Nonetheless, the absence of the W^{+5} oxidation state on the air-exposed surface could be caused by tungsten reoxidation by air, not excluding oxygen vacancies from the material bulk. The characteristic defect states that lie within the band gap of these non-stoichiometric TMOs were also identified near the Fermi level [28,29,30], although in a minor degree for WO_x (Fig. 2(d)).

Another feature of the studied TMOs is their peculiarly large work function (Φ_{TMO}) and how it changes as a result of redox environments, contamination by adsorbates and chemical interaction with adjacent interfaces [27]. In this sense, the Φ_{TMO} values after thermal evaporation will be several meV smaller than those of *in-situ* metal oxidation. Furthermore, as the oxides are exposed to ambient air, Φ_{TMO} will further decrease ~1 eV until stabilizing [32]. As indicated in Table 1, the reported work function values vary from Φ_{TMO} ~6–7 eV (as-deposited) to ~5.0–5.3 eV (after air-exposure). These values are close to the ionization potential of c-Si (5.1 eV), suggesting that Fermi level alignment between both materials is feasible. Accordingly, TMOs exhibit a double functionality depending on the relative work function difference Φ_{TMO}–Φ_{Si} of both materials [33]. For n-Si, these TMOs will induce an electrostatic potential (band bending) owing to a large Φ_{TMO}–$\Phi_{n\text{-}Si}$, depleting silicon's surface out of majority carriers (electrons) and acting as p-emitters. For p-Si, TMOs act as ohmic-like contacts given a small Φ_{TMO}–$\Phi_{p\text{-}Si}$, accumulating majority carriers (holes) in the surface and acting as p-BSFs. As it will be discussed in Section 3.3, this functionality occurs irrespectively of the n-type character of these oxides.

Finally, a benefic property of TMOs in general is a wider energy band gap (>3 eV) than conventional a-Si:H emitters (E_{gap} ~1.7 eV) (see Table 1). This translates into lower absorption losses in the near-ultraviolet and visible ranges when used as window layers [34]. Fig. 3 shows the optical absorbances measured by spectrophotometry, subtracting the contribution of the glass slide. By comparing with a-Si:H (calculated from extinction coefficient data [35]), all three oxides are less absorbent up to ~600 nm in wavelength, while MoO_x is the most transparent. In parallel, electrical measurements of the oxide films at room temperature yielded rather low lateral conductivities (σ_{V2Ox} ~8 x10^{-8} S/cm, σ_{MoOx} ~1.8 x10^{-7} S/cm and σ_{WOx} ~1.1 x10^{-7} S/cm) in accordance with previous reports [9,18]. These results limit the oxide thickness on the final device to only a few nanometers and justifies the need

for an ITO collecting electrode. Ultimately, actual conductivities will depend on the morphology of thermally-evaporated TMOs, which has been reported as completely amorphous for MoO_x [20] and nano-crystalline for WO_x [30]. Further study of preparation methods and post-deposition treatments could promote oxide crystallinity in order to enhance film conductivities.

Overall, the identification of oxygen-vacancy defects in the TMOs under study (at least for the V_2O_x and MoO_x cases), as well as their inherently large work functions (>5eV) and excellent optical transparency, strongly indicate that these materials possess the functionality required for carrier-selective contacts in c-Si heterojunctions. In the following, the aforementioned properties will be related to the operating conversion efficiency of finished solar cells with V_2O_x, MoO_x and WO_x as hole-selective contacts.

3.2 Transition Metal Oxide/n-Si Solar cells

Since TMO thickness is a critical design variable, preliminary solar cell devices were fabricated on flat wafers with varying MoO_x thicknesses (30, 60 and 90 nm). The obtained open-circuit voltages (V_{OC}) were almost invariant at 603 ±7 mV, suggesting that the capability of MoO_x to passivate silicon's surface does not depend on its thickness. In contrast, the short-circuit current densities (J_{SC}) decreased from 30.6 mA/cm^2 (30 nm) to 25.6 (90 nm) due to parasitic absorbance and reflectance losses of the MoO_x/ITO layers. Contrary to expectation, the Fill Factors (*FF* ~70%) and series resistances (R_S ~ 1.2 Ω·cm^2) remained relatively constant, indicating that transverse electrical conductance is still moderate for thicker oxide layers.

A compromise between optical and electrical losses was obtained for a MoO_x thickness of 15 nm and an ITO thickness of 80 nm, as determined by ray tracing modeling of the solar cell structure with *Wafer Ray Tracer* simulation tool [36], using a refractive index mismatch of n_{MoOx}/n_{ITO} = 2.1/2.0 (Fig. 4). Thinner ITO thicknesses could also be used but this would result in higher power losses due to excessive series resistance, given the quality of the ITO (130 Ω/sq) and the current finger grid design. By assuming a constant V_{OC} of 600 mV and a conservative *FF* of 70%, a maximum power conversion efficiency (*PCE*) of 16.9% was obtained. A MoO_x thickness of 15 nm also ensures an adequate layer uniformity (i.e. no pin-holes) over the surface area of a texturized substrate. Consequently, TMO thicknesses of 15 nm were also chosen for V_2O_x and WO_x, given their similar refractive indexes.

Fig. 5(a) shows the current density-voltage (*J*–*V*) response of the fabricated TMO/n-Si solar cells, measured under standard illumination conditions (AM1.5g solar spectrum, 1000 W/m^2) at 25 ºC. The best performance is achieved for V_2O_x with a *PCE* of 15.7% and a V_{OC} of 606 mV. It is followed by MoO_x (13.6%, 581mV) and WO_x (12.5%, 577 mV), whose reduced efficiencies are a result of lower V_{OC} and *FF* values. The underperformance of WO_x could be partially explained by the absence of oxygen vacancies or merely by its lower passivation potential. It is worth noting that these V_{OC}s are remarkable for such simplified structures, considering the thinness of the oxide film and the absence of a passivation interlayer. For comparison, a reference a-Si:H/c-Si heterojunction with good front surface passivation reaches a V_{OC} value of 685 mV. The measured series resistances (R_S = 0.72–1.5 Ω·cm^2) are moderate considering the high lateral resistivities of these films, resulting in modest *FF* values. A summary of the obtained solar cell parameters is shown in Table 2.

The short-circuit current densities are very similar for all devices, with a small variation between V_2O_x reaching a maximum of 34.4 mA/cm^2 and WO_x a minimum of 33.3 mA/cm^2. These J_{SC}s (4.3% grid shadow included) match the J_{SC} values obtained from the integration of the External Quantum Efficiency (EQE) response with the photon flux spectrum at AM1.5g. As can be observed in Fig. 5(b), all oxides show a substantial EQE improvement in the 300–600 nm range when compared to a-Si:H, accounting for a gain in photocurrent of 1.19 mA/cm^2. Moreover, V_2O_x shows an additional absorption feature between 800 and 1000 nm, possibly explained by its higher passivation quality.

A shortfall of silicon heterojunction solar cells is the passivation damage and V_{OC} loss induced by sputtering and e-beam evaporation [37]. In this sense, the contactless Quasi-Steady-State Photoconductance (QSSPC) [38] technique can be very useful to assess the intrinsic V_{OC} potential of undamaged device structures. In particular, the implicit open-circuit voltages (*i*-V_{OC}) measured before and after sputtering of the ITO layer are shown in Fig. 6. A notable *i*-V_{OC} of 631 mV is obtained for the V_2O_x device, enhancing the achievable conversion efficiency to 16.3% if no sputtering damage was present. A similar improvement is measured for MoO_x, while the effect on WO_x is less important. In standard a-Si:H/c-Si solar cells, the recovery of the V_{OC} is routinely done by post-fabrication thermal annealing (160 ºC for 20 minutes) [37], enhancing the current collection efficiency. However, the hereby

reported solar cells were not annealed after having observed *FF* absolute losses of 25–35%, attributed to TMO instabilities but needing further investigation.

Furthermore, by use of the methodology proposed by [39], we determined the emitter term of the saturation current density J_{0e} as a function of the effective lifetime τ_{eff}:

$$1/\tau_{eff} - 1/\tau_{bulk} - S_{rear}/W = J_{0e}(N_D + \Delta n)/qn_i^2 W \quad (1)$$

where q is the elementary charge, n_i the intrinsic carrier concentration in silicon, W the wafer thickness, N_D the wafer doping concentration and Δn the minority excess carrier density (under high injection conditions). The term $1/\tau_{bulk}$ can be neglected owing to the long bulk lifetime of high quality wafers, whereas the surface recombination velocity S_{rear} for the laser-fired a-Si:H/SiC:H stack was estimated at ~50 cm/s [26]. Hence, the characteristic emitter saturation currents for the TMOs are $J_{0\,V2Ox}$ ~150, $J_{0\,MoOx}$ ~230 and $J_{0\,WOx}$ ~420 fA/cm^2, which are close to the reported value of 300 fA/cm^2 for MoO_x/n-Si contacts [18]. These emitter saturation values are not far from boron-diffused state of the art technology (J_{0e} ~100 fA/cm^2), confirming the true potential of transition metal oxides as hole-selective contacts.

3.3 Origin of rectification in TMO/n-Si heterojunctions

In order to elucidate the carrier transport mechanism in TMO/n-Si heterojunctions, their dark *J–V* characteristics were measured at varying temperatures and fitted for the double diode solar cell model, extracting J_{01} and J_{02} for the diffusion and recombination diodes respectively (Fig. 7(a)). The thermally-activated behavior of each J_0 is defined by a specific activation energy (E_a) [34]:

$$J_0 = J_{00} \exp(-E_a/nkT) \quad (2)$$

where J_{00} is the saturation current pre-factor, kT the thermal voltage and n the ideality factor for each fitted diode (n_1 = 1 and n_2 = 2). From the exponential fit of the Arrhenius plots in Fig. 7(b), the obtained activation energies seem to be related to crystalline silicon´s bandgap ($E_{a1} = E_{gap}$, $E_{a2} = ½E_{gap}$). This result suggests that the *J–V* response is limited by diffusion of injected minority carriers (J_{01}) and recombination in the space-charge region (J_{02}), rather than alternative processes such as thermionic emission.

Based on the obtained J_0 (E_{gap}) dependence, the classical depletion approximation was then used to analyze the TMO/n-Si heterojunction. Parting from equilibrium conditions, the Fermi level difference between both semiconductors is distributed between the induced built-in

potential V_{bi} across the heterojunction and the dipole Δ that very likely occurs at the interface [33]:

$$\Phi_{MoOx} - \Phi_{n-Si} = qV_{bi} - \Delta \quad (3)$$

This V_{bi} is expected to be mostly allocated on the silicon bulk, given the thinness of the TMO layer. As mentioned before, the effect of the V_{bi} is a pronounced band bending of silicon's valence band up to the point of surface inversion, creating a p^+ contact appropriate for hole transfer, as depicted in Fig. 8. Similarly, up-bending of the conduction band creates a barrier for electrons, promoting the separation of photogenerated carriers. Assuming a strongly inverted surface potential $\psi_s = V_{bi} = 0.7$ V, solving of Eq. (2) gives a dipole of $\Delta \sim -0.5$ V, which accounts for negative trap charges in the TMO/n-Si interface. The presence of negative dipoles in TMOs has been previously reported, originating from shallow O vacancies and playing an important role in energy level alignment with several organic semiconductors [10,40,41]. Furthermore, given their n-type nature and their relatively low density of gap states, it can be argued that the transport of photogenerated holes across the oxide bulk does not occur, but instead they recombine in the TMO/n-Si interface with those electrons supplied by the ITO contact [42]. At any rate, further characterization of TMO/c-Si interfaces is needed to fully understand the charge-transfer mechanism of these devices.

4. Conclusion

Three n-type transition metal oxides (V_2O_x, MoO_x and WO_x) with work function values >5eV were effectively used as hole-selective contacts for n-Si heterojunction solar cells, obtaining a maximum V_{OC} of 606 mV for the V_2O_x/n-Si device with a corresponding *PCE* of 15.7%. After MoO_x (13.6%), the lowest performance was for WO_x (12.5%), possibly due to the absence of oxygen vacancies in its atomic structure as determined from XPS analyses. Even though high lateral resistivities were measured for these oxides, series resistances in the solar cells were moderate because of the thin layers utilized (15 nm). A wide energy band gap resulted in an estimated J_{SC} gain of ~1.2 mA/cm^2 (for 300–600 nm wavelengths) when compared to a reference a-Si:H emitter. Although diffusion of injected minority carriers appears to be the predominant transport process, questions remain regarding the specific extraction mechanism of photogenerated holes via gap states in these oxides. In future works, the possibility to include additional passivation interlayers to further increase V_{OC} values should be investigated. Additionally, a significant improvement could be achieved by fine-tuning the transition metal oxide work function (for instance, by avoiding air-exposure) or by eliminating the *i*-V_{OC} losses of ~20 mV caused by sputtering damage. Given the obtained

results, prospective applications of these doping-free heterojunctions could be extended to advanced silicon technologies such as ultra-thin wafers or interdigitated back-contacts, taking advantage of the demonstrated low-temperature and solution processability of transition metal oxides.

Acknowledgement

The authors would like to thank Montserrat Dominguez for the XPS analyses and Trifon Trifonov for the SEM measurements. This work has been supported by the Spanish government under project ENE2014-56237-C4. We are also thankful for financial collaboration from XaRMAE of the Generalitat de Catalunya.

References

[1] T. Yamaguchi, Y. Ichihashi, T. Mishima, N. Matsubara, T. Yamanishi, Achievement of more than 25 % conversion heterojunction solar cell, IEEE J. Photovoltaics. 4 (2014) 1433–1435.

[2] G. Li, R. Zhu, Y. Yang, Polymer solar cells, Nat. Photonics. 6 (2012) 153–161.

[3] K.A. Nagamatsu, S. Member, S. Avasthi, J. Jhaveri, J.C. Sturm, A 12 % efficient silicon/PEDOT:PSS heterojunction solar cell fabricated at <100°C, IEEE J. Photovoltaics 4 (2014) 260–264.

[4] D. Zielke, A. Pazidis, F. Werner, J. Schmidt, Organic-silicon heterojunction solar cells on n-type silicon wafers: The BackPEDOT concept, Sol. Energy Mater. Sol. Cells 131 (2014) 110–116.

[5] D. Zielke, C. Niehaves, W. Lövenich, A. Elschner, M. Hörteis, J. Schmidt, Organic-silicon solar cells exceeding 20 % efficiency, submitted to Proceedings of 5th International Conference on Silicon Photovoltaics (2015) (Konstanz, Germany).

[6] K. Kawano, R. Pacios, D. Poplavskyy, J. Nelson, D. Bradley, J.R. Durrant, Degradation of organic solar cells due to air exposure, Sol. Energy Mater. Sol. Cells 90 (2006) 3520–3530.

[7] S. Avasthi, S. Lee, Y.-L. Loo, and J. C. Sturm, Role of majority and minority carrier barriers silicon/organic hybrid heterojunction solar cells, Adv. Mater. 23 (2011) 5762–5766.

[8] V. V. Brus, M. Zellmeier, X. Zhang, S. M. Greil, M. Gluba, J. Töfflinger, et al., Electrical and photoelectrical properties of P3HT/n-Si hybrid organic–inorganic heterojunction solar cells, Org. Electron. 14 (2013) 3109–3116.

[9] J. Meyer, S. Hamwi, M. Kröger, W. Kowalsky, T. Riedl, A. Kahn, Transition metal oxides for organic electronics: energetics, device physics and applications, Adv. Mater. 24 (2012) 5408–27.

[10] F. Wang, Z. Tan, Y. Li, Solution-processable metal oxides/chelates as electrode buffer layers for efficient and stable polymer solar cells, Energy Environ. Sci. 8 (2015) 1059–1091.

[11] H. You, Y. Dai, Z. Zhang, D. Ma, Improved performances of organic light-emitting diodes with metal oxide as anode buffer, J. Appl. Phys. 101 (2007) 026105.

[12] J. Meyer, S. Hamwi, T. Bu□low, H.H. Johannes, T. Riedl, W. Kowalsky, Highly efficient simplified organic light emitting diodes, Appl. Phys. Lett. 91 (2007) 113506.

[13] G. Li, C.W. Chu, V. Shrotriya, J. Huang, Y. Yang, Efficient inverted polymer solar cells, Appl. Phys. Lett. 88 (2006) 253503.

[14] D.S. Leem, H.D. Park, J.W. Kang, J.H. Lee, J.W. Kim, J.J. Kim, Low driving voltage and high stability organic light-emitting diodes with rhenium oxide-doped hole transporting layer, Appl. Phys. Lett. 91 (2007) 011113.

[15] Y. Sun, C. J. Takacs, S. R. Cowan, J. H. Seo, X. Gong, A. Roy, et al., Efficient air-stable bulk heterojunction polymer solar cells using MoOx as the anode interfacial layer, Adv. Mater. 23 (2011) 2226–30.

[16] S. Il Park, S. Jae Baik, J.S. Im, L. Fang, J.W. Jeon, K. Su Lim, Towards a high efficiency amorphous silicon solar cell using molybdenum oxide as a window layer instead of conventional p-type amorphous silicon carbide, Appl. Phys. Lett. 99 (2011) 063504.

[17] G. Sno, M. Lif, Doping-Free Intrinsic Amorphous Silicon Thin-Film Solar Cell Having a Simple Structure of glass/SnO2/MoO3/i-a-Si/LiF/Al, IEEE Electron Device Lett. 35 (2014) 96–98.

[18] J. Bullock, A. Cuevas, T. Allen, C. Battaglia, Molybdenum oxide MoOx: a versatile hole contact for silicon solar cells, Appl. Phys. Lett. 105 (2014) 232109.

[19] A.B. Morales-Vilches, L.G. Gerling, J. Puigdollers, C. Voz, R. Alcubilla, Doping-free alternatives for passivated back-contacts in silicon heterojunctions solar cells, unpublished results presented at Materials Research Society spring meeting (2015) (San Francisco, USA).

[20] C. Battaglia, X. Yin, M. Zheng, I.D. Sharp, T. Chen, S. Mcdonnell, et al., Hole selective MoOx contact for silicon solar cells, Nano Lett. 14 (2014) 967–971.

[21] L. Ding, M. Boccard, Z.C. Holman, M.I. Bertoni, evaluation of transition metal oxides as carrier-selective contacts for silicon heterojunction solar cells, presented at Materials Research Society spring meeting (2015) (San Francisco, USA).

[22] M. Bivour, J. Temmler, H. Steinkemper, M. Hermle, Alternative contact materials for induced junction silicon solar sells, submitted to Proceedings of 5th International Conference on Silicon Photovoltaics (2015) (Konstanz, Germany).

[23] C. Battaglia, S.M. de Nicolás, S. De Wolf, X. Yin, M. Zheng, C. Ballif, et al., Silicon heterojunction solar cell with passivated hole selective MoOx contact, Appl. Phys. Lett. 104 (2014) 113902.

[24] K. Werner, The Evolution of silicon wafer cleaning technology, J. Electrochem. Soc. 137 (1990) 1887-1892.

[25] M.T. Greiner, L. Chai, M.G. Helander, W.M. Tang, Z.H. Lu, Metal/metal-oxide interfaces: how metal contacts affect the work function and band structure of MoO3, Adv. Funct. Mater. 23 (2013) 215–226.

[26] M. Colina, A. Bel, I. Mart, P.R. Ortega, R. Alcubilla, low surface recombination in silicon-heterojunction solar cells with rear laser-fired contacts from aluminum foils, IEEE J. Photovoltaics 5 (2015) 805–811.

[27] M.T. Greiner, Z.-H. Lu, Thin-film metal oxides in organic semiconductor devices: their electronic structures, work functions and interfaces, NPG Asia Mater. 5 (2013) e55.

[28] K. Zilberberg, S. Trost, J. Meyer, A. Kahn, A. Behrendt, D. Lützenkirchen-Hecht, et al., Inverted organic solar cells with sol-gel processed high work-function vanadium oxide hole-extraction layers, Adv. Funct. Mater. 21 (2011) 4776–4783.

[29] K. Kanai, K. Koizumi, S. Ouchi, Y. Tsukamoto, K. Sakanoue, Y. Ouchi, et al., Electronic structure of anode interface with molybdenum oxide buffer layer, Org. Electron. 11 (2010) 188–194.

[30] M. Vasilopoulou, L.C. Palilis, D.G. Georgiadou, A.M. Douvas, P. Argitis, S. Kennou, et al., Reduction of tungsten oxide: a path towards dual functionality utilization for efficient anode and cathode interfacial layers in organic light-emitting diodes, Adv. Funct. Mater. 21 (2011) 1489–1497.

[31] C.H. Cheung, W.J. Song, S.K. So, Role of air exposure in the improvement of injection efficiency of transition metal oxide/organic contact, Org. Electron. 11 (2010) 89–94.

[32] I. Irfan, A. James Turinske, Z. Bao, Y. Gao, Work function recovery of air exposed molybdenum oxide thin films, Appl. Phys. Lett. 101 (2012) 093305.

[33] J. Bisquert, Nanostructured energy devices: Equilibrium Concepts and Kinetics, CRC Press (2014).

[34] T. Dittrich, Materials Concepts for Solar Cells, Imperial College Press (2014).

[35] Z. Holman, A. Descoeudres, L. Barraud, F. Fernandez, J. Seif, S. De Wolf, C. Ballif, Current losses at the front of silicon heterojunction solar cells, IEEE J. Photovoltaics 2 (2012) 7–15.

[36] Wafer Ray Tracer simulation tool (Version 1.6.4). Online on www.pvlighthouse.com.au, Last accessed 5/25/2015.

[37] B. Demaurex, S. De Wolf, A. Descoeudres, Z. Charles Holman, C. Ballif, Damage at hydrogenated amorphous/crystalline silicon interfaces by indium tin oxide overlayer sputtering, Appl. Phys. Lett. 101 (2012) 171604.

[38] R.A. Sinton, A. Cuevas, Contactless determination of current–voltage characteristics and minority carrier lifetimes in semiconductors from quasi-steady-state photoconductance data, Appl. Phys. Lett. 69 (1996) 2510

[39] A. Cuevas, D. Macdonald, Measuring and interpreting the lifetime of silicon wafers, Solar Energy 76 (2004) 255–262.

[40] Y. Guo, J. Robertson, Origin of the high work function and high conductivity of MoO3, Appl. Phys. Lett. 105 (2014) 222110.

[41] Irfan, H. Ding, Y. Gao, D.Y. Kim, J. Subbiah, F. So, Energy level evolution of molybdenum trioxide interlayer between indium tin oxide and organic semiconductor, Appl. Phys. Lett. 96 (2010) 073304.

[42] J. Meyer, M. Kro□ger, S. Hamwi, F. Gnam, T. Riedl, W. Kowalsky, et al., Charge generation layers comprising transition metal-oxide/organic interfaces: electronic structure and charge generation mechanism, Appl. Phys. Lett. 96 (2010) 193302.

List of tables

Table 1 Peak positions (eV) of fitted XPS spectra and relative content of each oxidation state identified, including O/M ratios and reported work functions (Φ_{TMO}) for as-deposited and air-exposed oxides. The oxidation state transitions $M^n \rightarrow M^{n-x}$ identified for each transition metal were $V^{+5} \rightarrow V^{+4}$, $Mo^{+6} \rightarrow Mo^{+5}$ and $W^{+6} \rightarrow W^{+5}$. Note also the energy band gap (E_{gap}) sensitivity to redox conditions.

Table 2 Photovoltaic parameters obtained for the fabricated solar cells with transition metal oxides (15 nm) as hole-selective contacts, compared to a reference heterojunction device with a-Si:H emitter.

List of figures

Highlights

- Transition metal oxide/n-crystalline silicon solar cells were fabricated.
- V_2O_x, MoO_x and WO_x were obtained after thermal evaporation under vacuum.
- XPS analyses revealed the presence of oxygen vacancies and/or gap states.
- Highest efficiency (open-circuit voltage) was 15.7% (606 mV) for V_2O_x/silicon.
- Current-voltage response is limited by diffusion of injected minority carriers.

Graphical Abstract

Click here to view linked References

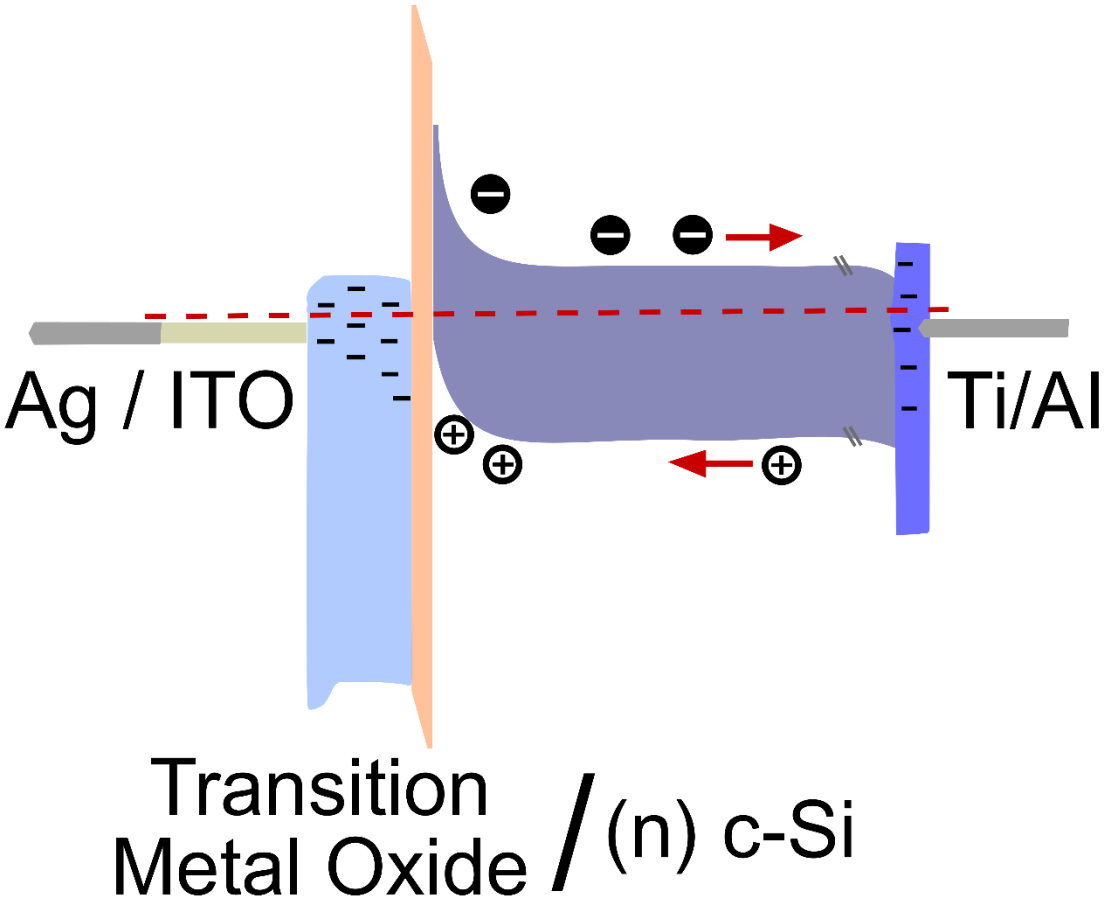

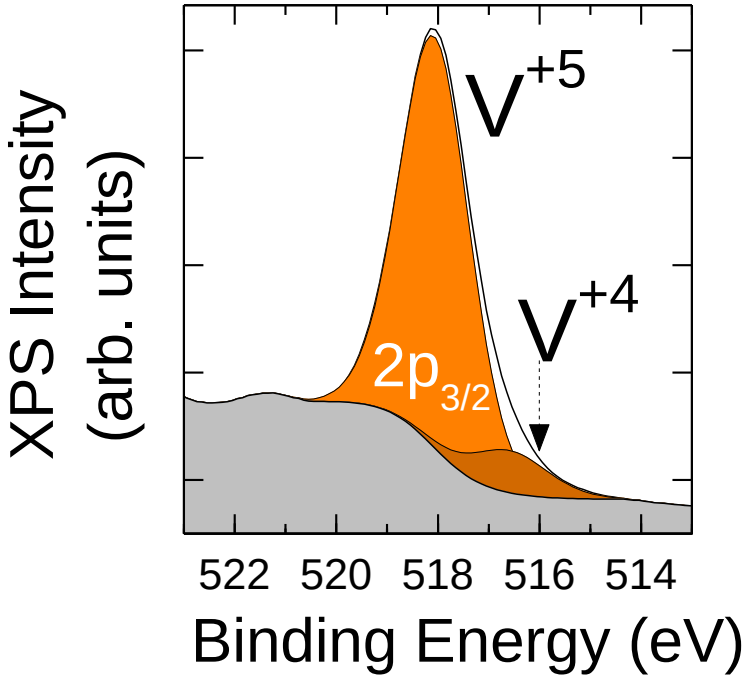

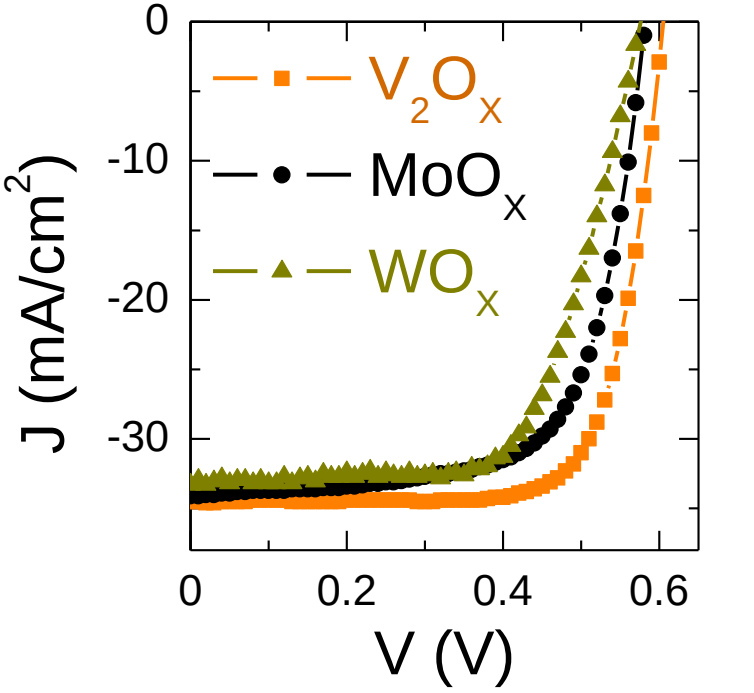

Tables

TMO	Core level peaks (eV)			Content (%)			O/M ratio	Φ_{TMO} (eV) / E_{gap} (eV)	
	Transition	M^n	M^{n-x}	M^n	M^{n-x}	O1s		As-deposited	Air-exposed
V_2O_x	V2$p_{3/2}$	518.1	516.6	27.3	3.1	69.6	2.3	7 / 2.8	5.3 / 3.6 [28]
	V2$p_{1/2}$	525.7	524.2						
MoO_x	Mo3$d_{5/2}$	233.4	231.8	28.1	0.5	71.4	2.5	6.7 / 3.2	5.4 / 3.2 [32]
	Mo3$d_{3/2}$	236.5	234.9						
WO_x	W4$f_{7/2}$	36.8	34.8	23.6	<0.1	76.4	3.2	6 / 3.1	5.0 / 3.1 [30]
	W4$f_{5/2}$	38.9	37.0						

Table 1

Peak positions (eV) of fitted XPS spectra and relative content of each oxidation state identified, including O/M ratios and reported work functions (Φ_{TMO}) for as-deposited and air-exposed oxides. The oxidation state variations $M^n \rightarrow M^{n-x}$ identified for each transition metal were $V^{+5} \rightarrow V^{+4}$, $Mo^{+6} \rightarrow Mo^{+5}$ and $W^{+6} \rightarrow W^{+5}$. Note also the energy band gap (E_{gap}) sensitivity to redox conditions.

Hole contact	V_{OC} (mV)	J_{SC} (mA/cm^2)	FF (%)	R_S (Ω·cm^2)	R_P (kΩ·cm^2)	PCE (%)
V_2O_x	606	34.4	75.3	0.72	440	15.7
MoO_x	581	34.1	68.8	0.84	80	13.6
WO_x	577	33.3	65.0	1.51	75	12.5
a-Si:H	685	34.4	77.6	0.67	570	18.3

Table 2

Photovoltaic parameters obtained for the fabricated solar cells with transition metal oxides (15 nm) as hole-selective contacts, compared to a reference heterojunction device with a-Si:H emitter.

Fig. 1 (140 mm width)

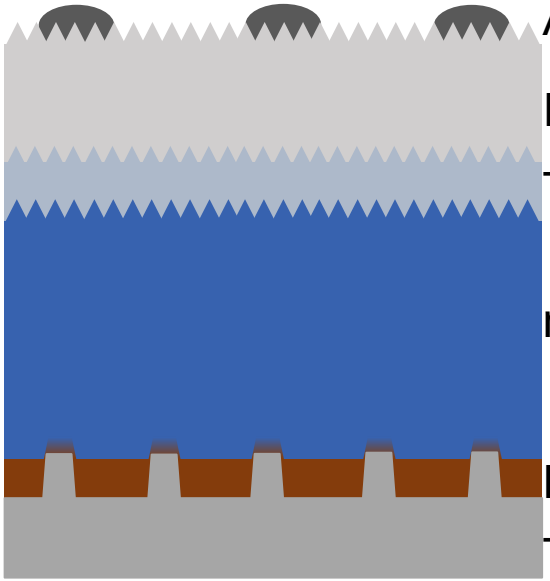

Ag (3 μm)

Indium-tin oxide (80 nm)

Transition metal oxide (15 nm)

n-type c-Si (0.5 Ω·cm, 280 μm)

Passivation/Back-reflector (100 nm)

Titanium (15nm)/Aluminum (1 μm)

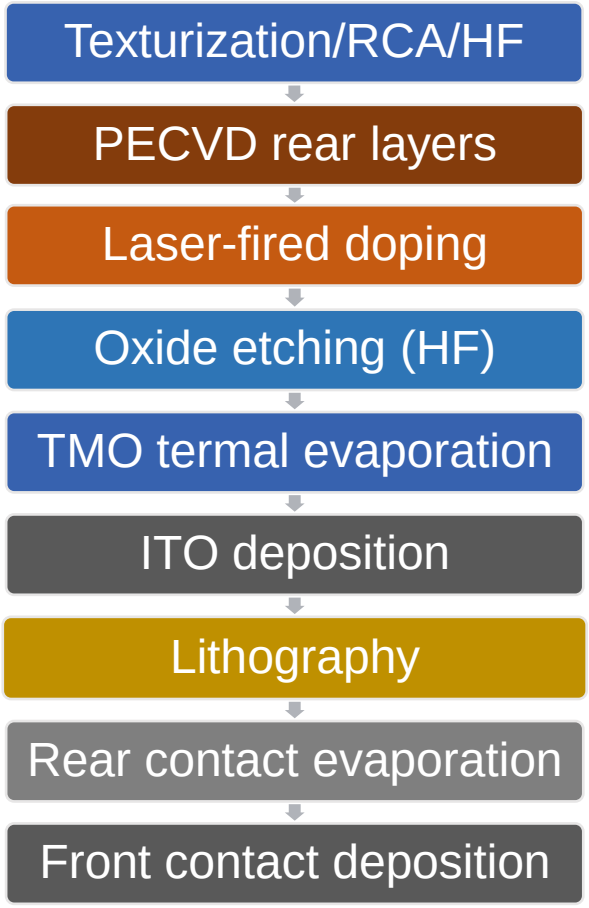

Fig. 2 (140 mm width)

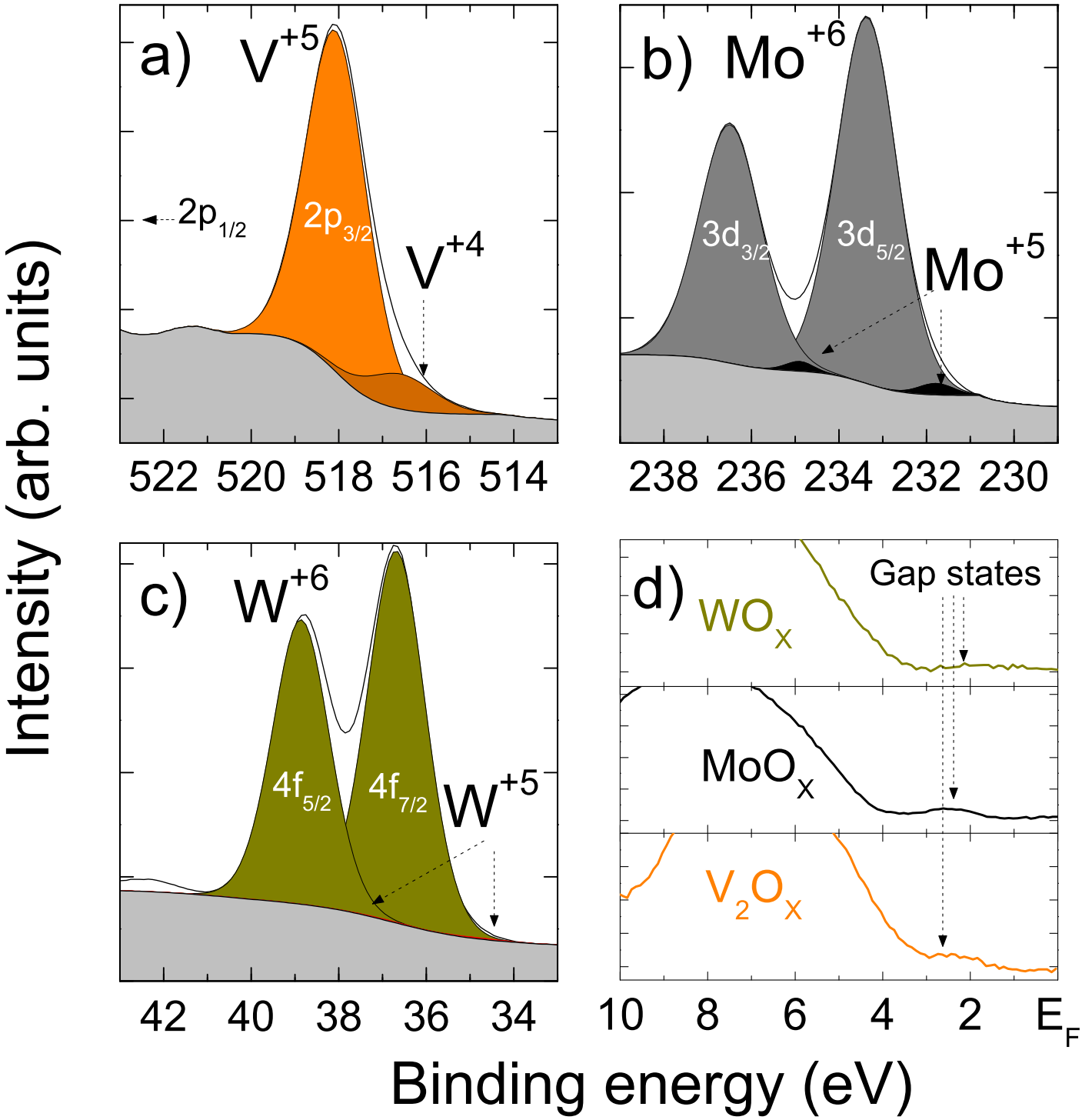

Fig. 3 (90 mm width)

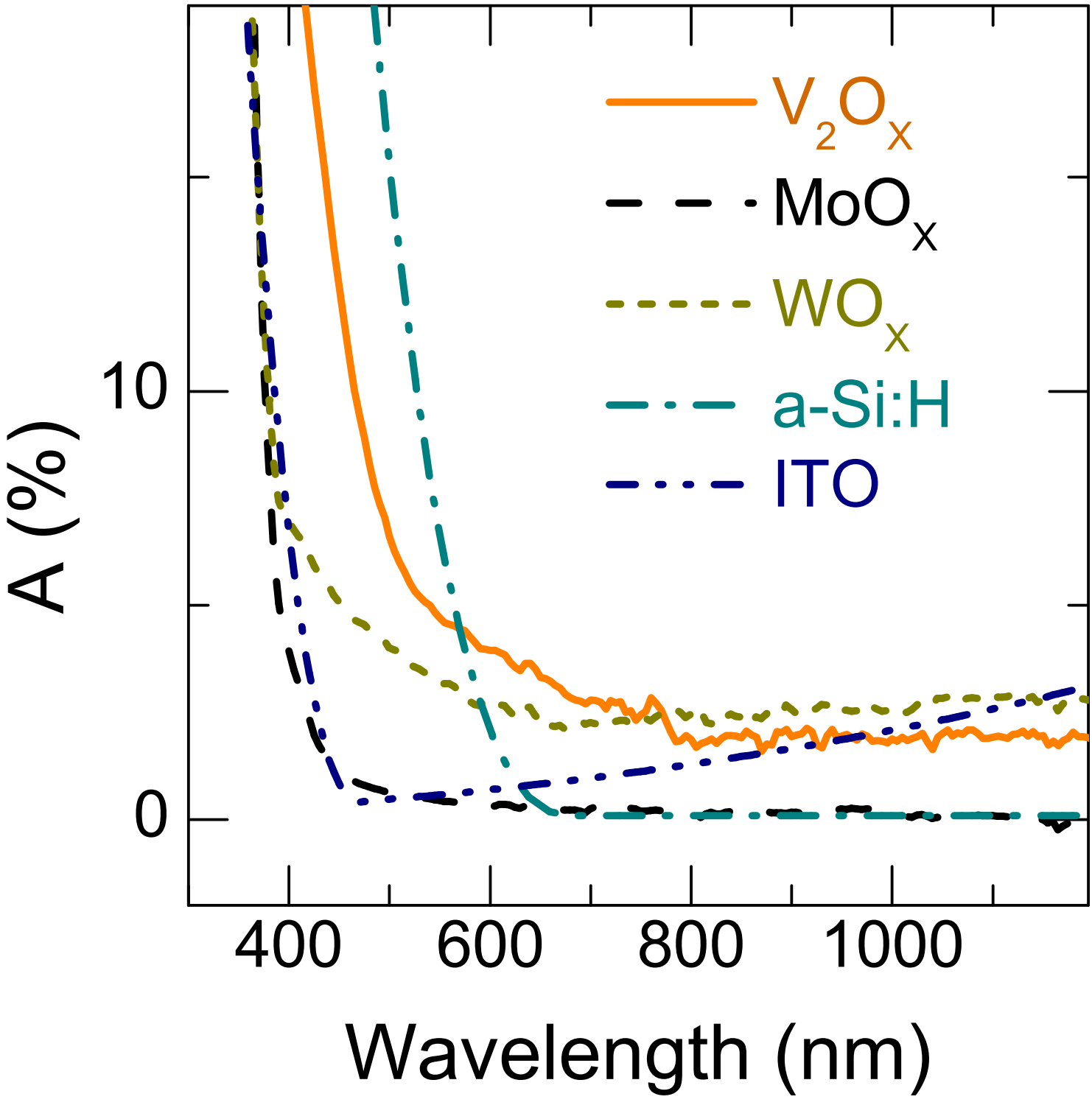

Fig. 4 (90 mm width)

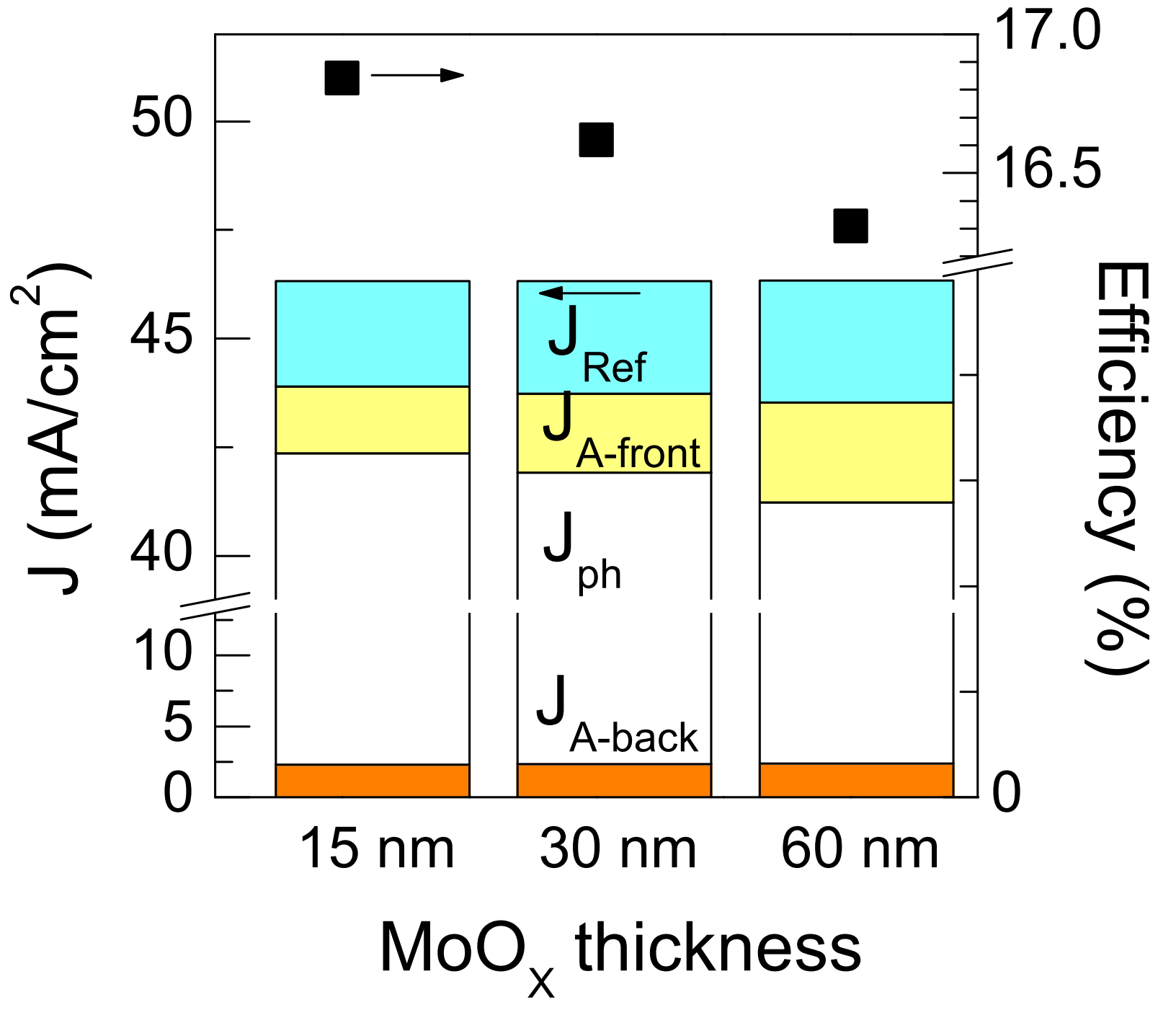

Fig. 5(a) (90 mm width)

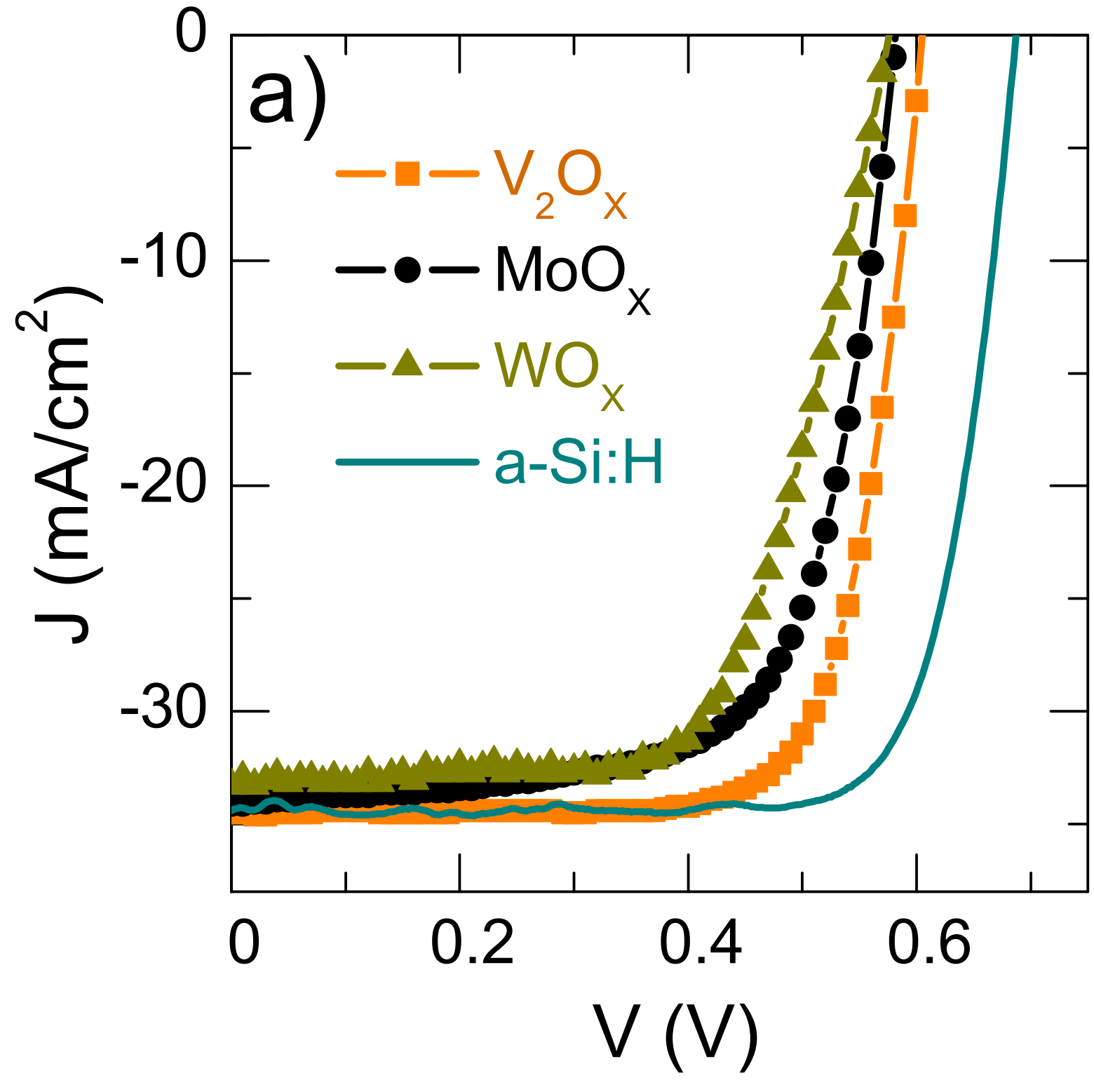

Fig. 5(b) (90 mm width)

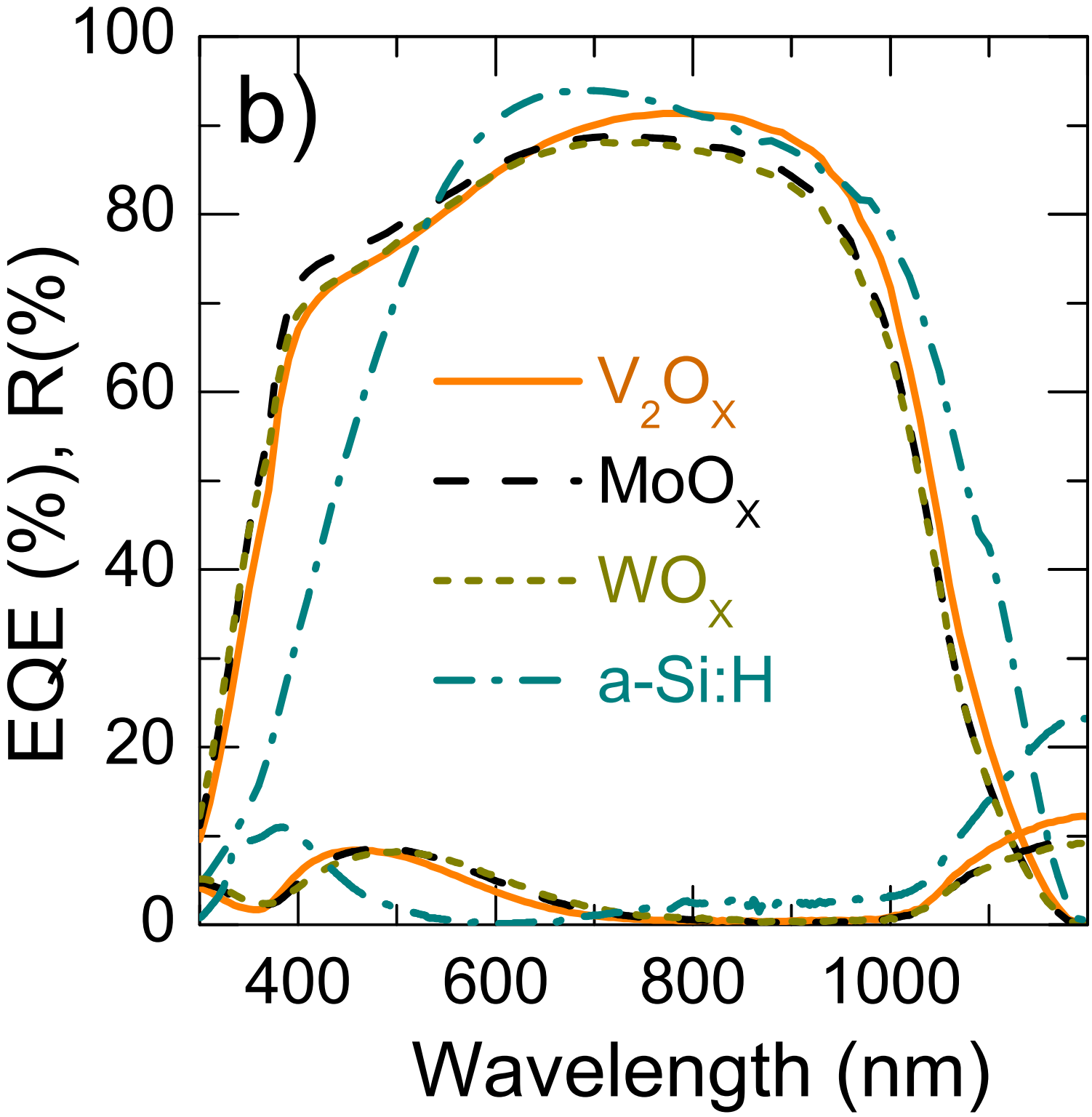

Fig. 6 (90 mm width)

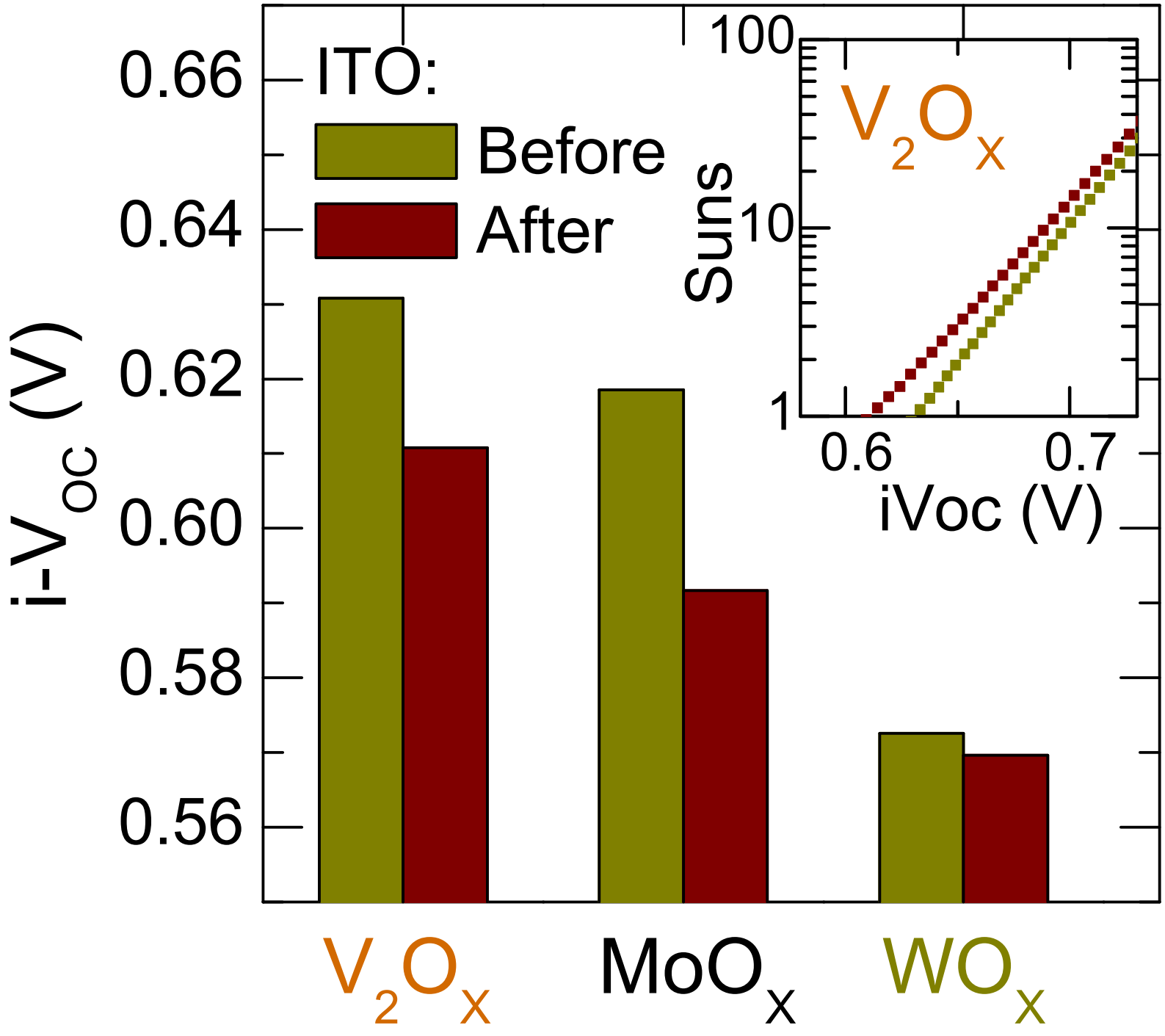

Fig. 7(a) (90 mm width)

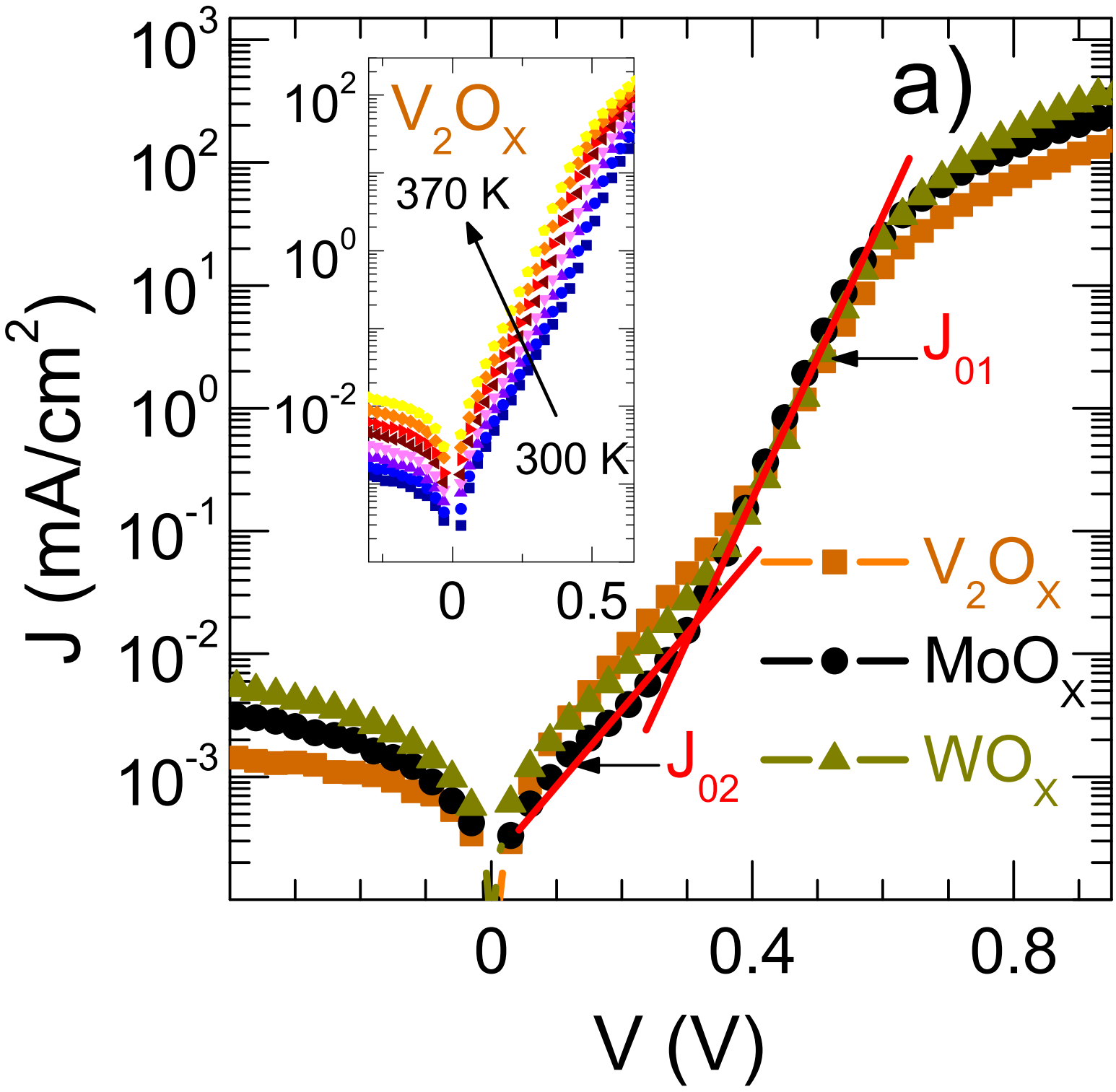

Fig. 7(b) (90 mm width)

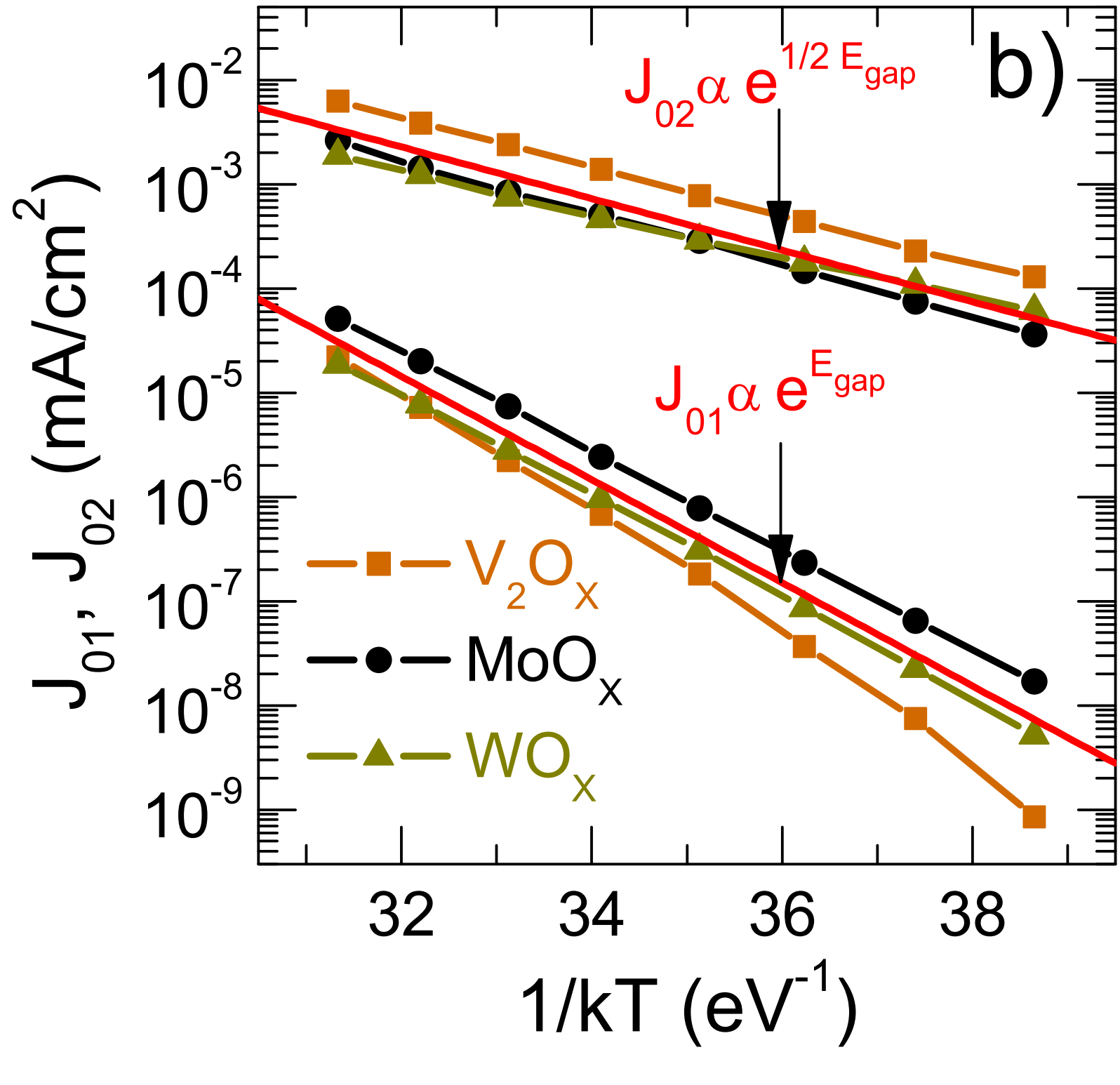

Fig. 8 (90 mm width)